Letter

Nonlinear ablative Rayleigh-Taylor instability: Increased growth due to self-generated magnetic fields

C. A. Walsh* and D. S. Clark
Lawrence Livermore National Laboratory, Livermore, California 94550, USA

(Received 15 August 2022; accepted 17 January 2023; published 27 January 2023)

The growth rate of the nonlinear ablative Rayleigh-Taylor (RT) instability is enhanced by magnetic fields self-generated by the Biermann battery mechanism; a scaling for this effect with perturbation height and wavelength is proposed and validated with extended-magnetohydrodynamic simulations. The magnetic flux generation rate around a single RT spike is found to scale with the spike height. The Hall parameter, which quantifies electron magnetization, is found to be strongly enhanced for short-wavelength spikes due to Nernst compression of the magnetic field at the spike tip. The impact of the magnetic field on spike growth is through both the suppressed thermal conduction into the unstable spike and the Righi-Leduc heat flow deflecting heat from the spike tip to the base. Righi-Leduc is found to be the dominant effect for small Hall parameters, while suppressed thermal conduction dominates for large Hall parameters. These results demonstrate the importance of considering magnetic fields in all perturbed inertial confinement fusion hot spots.

DOI: 10.1103/PhysRevE.107.L013201

The Rayleigh-Taylor instability [1–3] (RTI) results in spike-bubble growth when a light fluid is accelerated into a dense fluid. The instability is prevalent in astrophysics [4–7] as well as laboratory plasma experiments, such as the acceleration [8–12] and deceleration [13–16] phases of inertial confinement fusion (ICF) implosions. In ICF experiments, the RTI is seeded by target imperfections [17–21] or asymmetries in the drive [22–24]. RTI growth is lowered when a transfer of energy (for example, electron heat flow or radiation) results in ablation of the dense spikes, which is called the ablative Rayleigh-Taylor instability (ARTI) [15,25–29].

Magnetic fields are anticipated to be self-generated at perturbations by the Biermann battery mechanism, both during acceleration of the ablator [30–34] and during the deceleration of the fusion fuel [35–37]. Magnetic fields up to 10 kT are expected in the hot spot, which is large enough to magnetize the electron population [35]. Previous ICF capsule simulations demonstrated that electron magnetization could enhance the growth of a perturbation by 7 μm within a hot spot of 30 μm radius [38]. While a theory for self-generated magnetic fields has been developed for the linear stage relevant to the acceleration phase of ICF implosions [39], the understanding of how magnetic fields affect different wavelengths or amplitudes of ARTI in the highly nonlinear deceleration phase remains lacking.

This Letter proposes an improved theory for the ARTI that includes the effect of self-generated magnetic fields. The theory is derived in three stages: magnetic flux quantification; magnetic flux concentration at spike tips; and thermal conduction magnetization. The change to the ARTI spike velocity due to extended magnetohydrodynamics (xMHD) will be demonstrated to be

$$\Delta V_{\mathrm{MHD}} \sim V_{\mathrm{abl}} \frac{\kappa_{\parallel}^{c} + \kappa_{\wedge}^{c} - \kappa_{\perp}^{c}}{\kappa_{\parallel}^{c}}, \tag{1}$$

where V_{abl} is the ablation velocity of cold fuel due to electron thermal conduction. The κ^c coefficients are thermal conductivity components [40], depending on the plasma ionization (Z) and the electron Hall parameter ($\omega_e \tau_e$). It will be shown that the scaling for $\omega_e \tau_e$ with spike height (h) and wavelength (λ) is

$$\omega_e \tau_e \sim \frac{h \int h \delta t}{\lambda^2}. \tag{2}$$

Simulations of a simplified ARTI test problem demonstrate the validity of the proposed theory. For this, the xMHD GORGON code [35,41,42] is used. GORGON includes magnetic fields self-generated through the Biermann battery process [35,43] as well as through composition gradients [44]. Kinetic suppression of the Biermann battery generation rate is included [45,46], although the results of this Letter are too collisional to be affected by this term. The transport of magnetic fields includes bulk plasma advection, Nernst, cross-gradient Nernst, and resistive effects [47]. In this Letter the magnetic field only feeds back on the plasma through magnetization of the electrons, as the magnetic pressure is insignificant. Magnetization of the electrons uses an anisotropic thermal conduction algorithm [48], including Righi-Leduc heat flow [49]. GORGON treats the electron and ion temperatures separately. Updated magnetized transport coefficients are used [34,50], which have been shown to affect spike propagation [38]. The equation of state utilized is the Frankfurt equation of state (FEOS) [51].

The ARTI test problem is the same as has been used previously to investigate the impact of an applied magnetic field on instability growth [52]. A light ($\rho_{L0} = 10^3$ kg/m^3)

*walsh34@llnl.gov

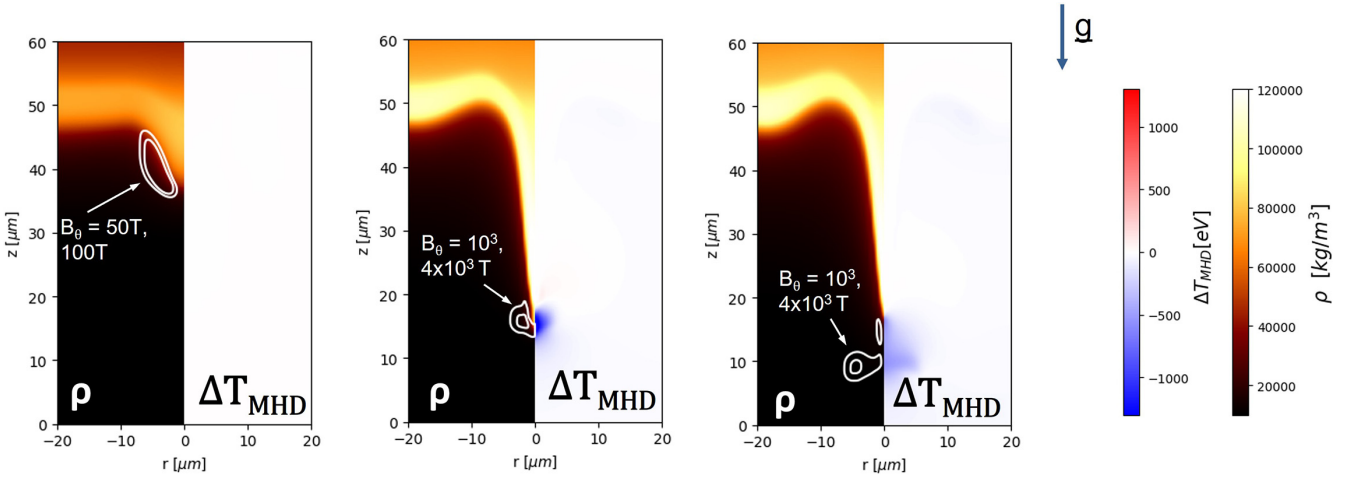

FIG. 1. Density and change in temperature due to MHD effects at three different times during the ARTI evolution for a perturbation of 20 μm wavelength. Select magnetic field strength contours have been indicated. The change in temperature due to MHD is calculated by taking the electron temperature profile with MHD and subtracting the temperature of a separate simulation with no MHD included.

deuterium-tritium (DT) plasma is accelerated ($g = 10^{15}$ m/s^2) into a dense DT plasma ($\rho_{H0} = 10^4$ kg/m^3). The system is initialized at rest with a transition layer ($d = 200$ μm) such that the density decays exponentially between ρ_{H0} and ρ_{L0}. The low-density DT plasma is initialized at $T_0 = 200$ eV for both ions and electrons, with the temperature elsewhere set such that the system is isobaric. Two-dimensional (2D) cylindrical ($r - z$) simulations are utilized, with the spike propagating down z. The grid resolution is kept at 0.5 μm for all cases; convergence tests were carried out, finding that additional resolution did not alter the agreement between simulations and theory.

The system inputs (g, ρ_{L0}, ρ_{H0}, T_0, d) have been chosen to mimic hot-spot conditions, with the hot plasma reaching 2.4 keV, 40 μm from the peak density location ($\rho \approx 1.2 \times 10^5$ kg/m^3) at $t = 1.5$ ns. This temperature increases to 3 keV by $t = 1.8$ ns as the hot plasma compresses up against the cold plasma. The spike height h is defined by the position of the 1 keV electron temperature contour.

A perturbation is applied at $t = 0$ by offsetting the density transition layer by $(h_0/2d)\cos[\min(\pi, 2\pi r/\lambda)]$ along the acceleration axis, where h_0 is the designated initial perturbation size. Note that for $r > \lambda/2$ the density transition does not vary with radius, meaning that the simulated perturbation is best conceptualized as an isolated spike, rather than a recurring sinusoidal perturbation. An isolated spike was chosen as it relates most strongly to capsule simulations motivating this work [38]. The radial boundary is set as $r = \lambda$ and the axial extent is 630 μm in all cases. The boundary conditions are transmissive everywhere except for $r = 0$, which is reflective. Throughout this Letter, the "small" perturbation case uses $h_0 = 0.2$ μm and the "large" perturbation case uses $h_0 = 0.5$ μm. Note that the initialized perturbation can be smaller than the grid size, as the interface is a smooth exponential decay in density over 200 μm.

The system is initialized as unmagnetized. This is valid, as the magnetic flux generation is weak during the linear RT evolution [37].

Figure 1 shows the evolution for perturbation wavelength $\lambda = 20$ μm and large initial height. Contours of magnetic field strength are indicated over the plasma density, with the change in electron temperature due to the self-generated magnetic fields shown on the right-hand side. At $t = 1.2$ ns the magnetic field has grown to over 100 T, but there is no significant change to the case where MHD is ignored. At 1.7 ns the magnetic field, which is primarily bunched around the spike tip, has grown to over 4 kT; at this level the MHD has reduced the temperature near the spike tip by over 1 keV. At 1.8 ns the magnetic field has detached from the spike tip and is propagating into the hot plasma, a process called magnetic flux injection. Up until this time the impact of MHD continually increases. Once injection takes place the impact of MHD on spike growth decreases. The theory in this Letter is only applicable while the magnetic field remains attached to the spike.

The first stage in the theory is quantifying the amount of magnetic flux around a perturbation. For a system with closed boundaries, the change in magnetic flux with time is [37]

$$\frac{\partial \Phi_B}{\partial t} = \oint \frac{\nabla P_e}{e n_e} \cdot \delta \underline{l} - \oint \frac{\beta_\parallel \nabla T_e}{e} \cdot \delta \underline{l}, \tag{3}$$

where $\underline{l}$ is the path along the boundary.

The two terms in Eq. (3) are sources of magnetic field. $\nabla P_e / e n_e$ is the Biermann battery effect and $-\beta_\parallel \nabla T_e / e$ is a corrective term for gradients in Z [44], although this is insignificant for the system of interest in this Letter [37].

Previous work studied the growth of magnetic flux in capsule simulations due to the Biermann battery effect, finding the following relation for a single-mode case [37],

$$\frac{\partial \Phi_B}{\partial t} = \frac{T_h - T_c}{e} \ln \frac{\rho_c}{\rho_h} \left(\frac{\Delta \rho R}{\rho R} - \frac{\Delta TR}{TR} \right), \tag{4}$$

where ρR is the line-integrated density, TR is the line-integrated temperature, and Δ is the single-mode variation due to the perturbation. T_h, T_c, ρ_h, and ρ_c are bulk temperatures and densities of the hot and cold regions. This equation was found to compare favorably with full extended-MHD simulations of ICF hot spots [37].

Equation (4) can be simplified further by noting that $\Delta \rho R \approx h(\rho_c - \rho_h)$ and $\Delta TR \approx h(T_c - T_h)$, which gives a

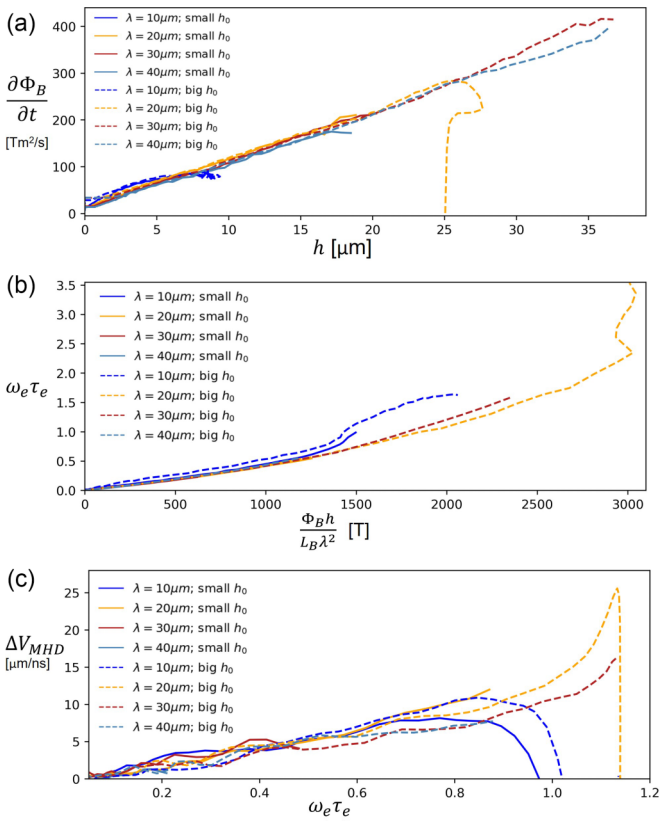

FIG. 2. These three figures demonstrate the effectiveness of the scalings proposed in this Letter by comparison with xMHD simulations with different perturbation wavelengths and initial heights. (a) is for the magnetic flux generation [Eq. (5)]; (b) is for the compression of magnetic flux at the spike tip [Eq. (8)]; (c) is for the impact of magnetization on the spike velocity [Eq. (1)].

scaling for magnetic flux generation,

$$\frac{\partial \Phi_B}{\partial t} \sim h, \tag{5}$$

i.e., the flux generation rate is independent of perturbation wavelength. Note that the domain size is changing when considering different perturbation wavelengths; if instead a whole capsule surface is considered, then more magnetic flux would result from the surface being filled with short-wavelength features rather than long wavelength of the same amplitude. However, the flux per feature would be the same.

Figure 2(a) plots the magnetic flux generation rate against spike height for simulations with different wavelengths and initial perturbation sizes, showing a good correlation until the magnetic flux injection regime is reached. Once the magnetic flux detaches from the spike, there can be significant resistive diffusion across the axis, resulting in the annihilation of flux.

Next, theory is developed to show how the magnetic field is concentrated at the spike tip. The transport of magnetic fields in an xMHD plasma is governed by the following equation [47],

$$\frac{\partial \underline{B}}{\partial t} = -\nabla \times \frac{\eta}{\mu_0} \nabla \times \underline{B} + \nabla \times (\underline{v}_B \times \underline{B}) + \nabla \times \left(\frac{\nabla P_e}{e n_e} - \frac{\beta_\parallel \nabla T_e}{e} \right), \tag{6}$$

where the first term on the right-hand side is resistive diffusion with diffusivity η and the second term is advection of the magnetic field at velocity $\underline{v}_B$,

$$\underline{v}_B = \underline{v} - \gamma_\perp \nabla T_e - \gamma_\wedge (\hat{\underline{b}} \times \nabla T_e), \tag{7}$$

where the current-driven terms [53] have been neglected due to their insignificance in this regime [47]. $\underline{v}$ is the bulk plasma velocity, while the $\gamma_\perp$ and $\gamma_\wedge$ terms are the Nernst and cross-gradient Nernst terms, respectively. $\hat{\underline{b}}$ is the magnetic field unit vector.

If the magnetic flux was evenly distributed along the perturbation surface, then the magnetic field strength would be approximately $\Phi_B/\lambda L_B$, where L_B is the magnetic field length scale into the spike. L_B is set primarily by Nernst advection of the magnetic field along the acceleration axis from hot to cold plasma, which is independent of perturbation wavelength or amplitude; indeed, $L_B \approx 4$ μm for all cases simulated. However, the peak field strength is found to be much larger than $\Phi_B/\lambda L_B$ for all cases and is dependent on the radial advection of magnetic field by Nernst into the spike tip. The ratio of radial Nernst advection (which compresses the flux) to the axial Nernst advection scales with h/λ. Assuming that this is the factor by which the magnetic flux compresses gives the electron magnetization scaling as

$$\omega_e \tau_e \sim \frac{\Phi_B h}{L_B \lambda^2}, \tag{8}$$

where $\omega_e\tau_e \sim |\underline{B}| T_e^{3/2}/n_e$. Equation (8) is compared with simulations in Fig. 2(b). While Fig. 2(a) shows that the magnetic flux generation rate decreases when the RT spikes reach the flux injection regime, the electron magnetization actually increases, as the magnetic fields are transported to a higher-temperature, lower-density plasma that is easier to magnetize. The overall equation for thermal conduction magnetization [Eq. (2)] is reached by combining Eqs. (5) and (8). Nernst has been confirmed as the cause of the additional h/λ dependence in Eq. (8) by artificially reducing only the radial component, which results in the expected reduction to electron magnetization.

Finally, with an understanding developed for how the magnetic field bunches at the spike tip, it is possible to turn our attention to how the magnetic field feeds back on the plasma hydrodynamics; this is not done directly through the magnetic pressure (the plasma β is too large in all cases), but instead through magnetization of the electron population. Magnetized electron heat flow follows,

$$\underline{q}_e = -\kappa_\parallel \nabla_\parallel T_e - -\kappa_\perp \nabla_\perp T_e - \kappa_\wedge \hat{\underline{b}} \times \nabla T_e, \tag{9}$$

where $\kappa_\parallel$ is the unmagnetized thermal conductivity along field lines; $\kappa_\perp$ is the thermal conductivity perpendicular to field lines that decreases with $\omega_e\tau_e$; $\kappa_\wedge$ is the Righi-Leduc coefficient. Righi-Leduc represents the electron heat flow being redirected 90° due to the magnetic field and peaks for $\omega_e\tau_e \approx 0.5$ in a DT plasma [40]. Note the similarities between this equation and the magnetic field advection velocity [Eq. (7)].

As the magnetic field is generated azimuthally in this 2D case, there is no component of heat flow along magnetic field lines [35]. Figure 3 shows the change in temperature at 1.7 ns

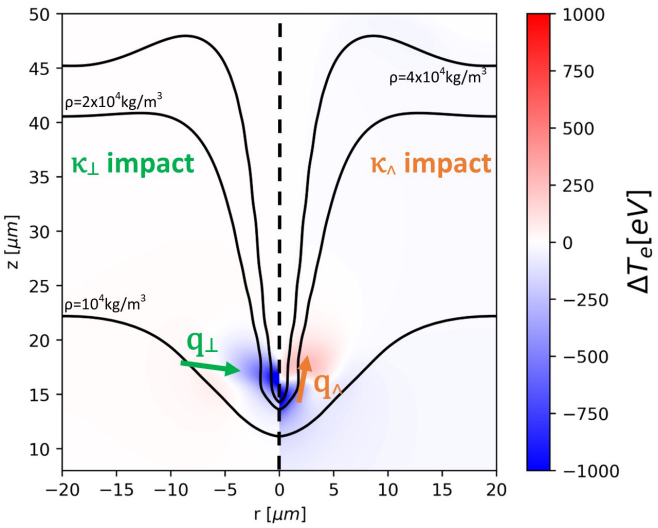

FIG. 3. Change in electron temperature of a $\lambda = 20$ μm spike due to magnetized thermal conduction (left) and Righi-Leduc heat flow (right). The left-hand plot is the difference in temperature between a simulation with magnetized heat flow ($\kappa_\perp$) and a simulation with purely unmagnetized heat flow ($\kappa_\parallel$). The plot on the right-hand side is the difference in temperature between simulations with and without Righi-Leduc heat flow turned on (where both simulations use magnetized heat flow $\kappa_\perp$). Density contours for the case including full MHD have been overlaid.

for the $\lambda = 20$ μm case due to both the magnetized perpendicular conduction ($\kappa_\perp$) and Righi-Leduc ($\kappa_\wedge$). The left-hand side of the figure is the effect of turning on the magnetized perpendicular thermal conduction, while the right-hand side is the additional effect once Righi-Leduc is turned on (for physical consistency, the cross-gradient Nernst advection of magnetic field is only included when Righi-Leduc is turned on [38]). The lowered value of $\kappa_\perp$ near the spike due to the magnetic field reduces the heat flow into the spike, cooling the tip. Righi-Leduc redirects heat flow down from the tip of the spike, also cooling the tip. In this case the two terms are contributing a similar amount to the overall change in electron temperature, although this is not true for all cases analyzed.

The stabilization of RT spikes scales with the ablation velocity of the spikes [15]. Here, we assume that the only process causing ablation is the electron heat flow. The ablation velocity can be obtained by assuming that all of the electron energy going into the cold fuel is then ablated into the hot spot [15], giving $V_{\rm abl} \sim \frac{\kappa_\parallel^c T_e^{5/2}}{L_T \rho}$ for the unmagnetized case. In this Letter it is proposed to replace the unmagnetized conductivity $\kappa_\parallel^c$ with the magnetized $\kappa_\perp^c$ and introduce an additional Righi-Leduc heat flow that reduces ablation at the spike tip. Therefore, the RT stabilization including magnetic fields is

$$V_{\rm MHD} \sim \frac{(\kappa_\perp^c - \kappa_\wedge^c) T_e^{5/2}}{L_T \rho}, \tag{10}$$

i.e., the change in spike velocity due to magnetic fields is as given in Eq. (1). The composite function of different κ^c coefficients is given in Fig. 4 for varying Hall parameters, showing that the Righi-Leduc term dominates at low $\omega_e \tau_e$, but the suppressed thermal conduction has a greater impact for $\omega_e \tau_e > 0.5$.

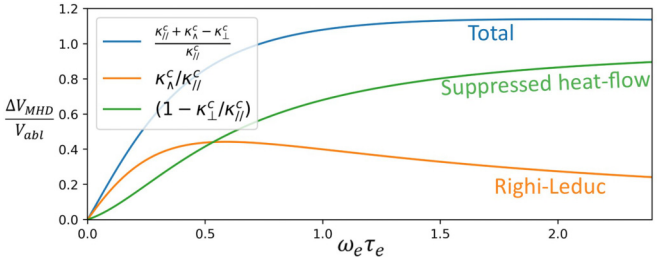

FIG. 4. Increase in RT spike velocity with electron magnetization, including separate curves showing the impact of suppressed perpendicular conduction and the Righi-Leduc component.

A comparison of Eq. (1) to the simulations is given in Fig. 2(c) with significant deviations from the scaling only when magnetic flux injection occurs.

Figure 5 shows the difference between spike height in simulations with MHD to cases without MHD. The impact of MHD continually increases in time until the spike is effectively stabilized, which allows for the magnetic field to detach from the spike. As the perturbation wavelength is decreased, the magnetic fields enhance the instability earlier in time, due to the $1/\lambda^2$ dependence of the magnetization from Eq. (2). However, the shorter wavelengths are also stabilized at an earlier time, which decreases the maximum impact of MHD. The large initial perturbation cases in Fig. 5 show that a $\lambda = 10$ μm spike has its propagation enhanced by 1.6 μm by 1.55 ns, before the spike is stabilized. For the $\lambda = 20$ μm case, however, the spike (and magnetic flux) continues to grow past 1.7 ns, by which time the MHD has enhanced the spike growth by 3.5 μm. This demonstrates the importance of the electron magnetization scaling with $h \int h \delta t$ from Eq. (2). The fractional change in spike height has also been calculated, giving maximum values of 20% for the $\lambda = 10$ μm case and 16% for $\lambda = 20$ μm. Maximum $\Delta h_{\rm MHD}/h$ is not found to decrease for smaller initial perturbations, although the peak is delayed in time.

In summary, a scaling for the enhancement of the nonlinear ablative Rayleigh-Taylor instability due to self-generated

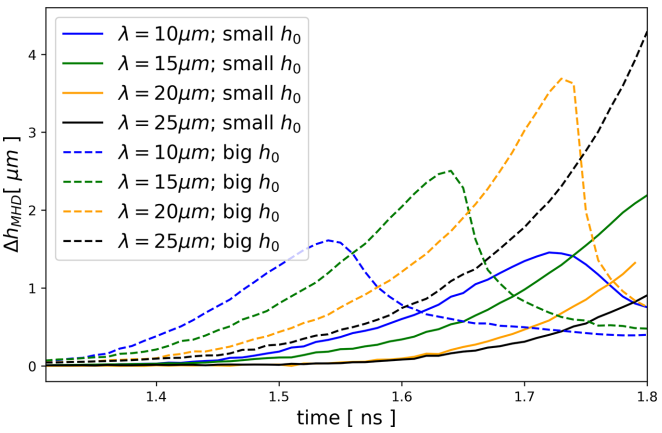

FIG. 5. Increase in spike height vs time due to self-generated magnetic fields for a number of perturbation wavelengths and initialized heights.

magnetic fields has been presented, comparing favorably with 2D extended-MHD results.

The theory can be used to postprocess capsule simulations to estimate the impact of magnetic fields. To demonstrate this, 2D capsule simulations of high-density-carbon (HDC) implosion N170601 are used with multimode shell thickness asymmetries. Previous work quantifying magnetic flux generation predicted peak flux for modes 40–60 [37]. Using the theory developed in this Letter, the dependence of electron magnetization on mode number can now be estimated, with peak magnetization for modes 20–35. The peak Hall parameter is calculated as up to 0.8, which results in $\Delta V_{\mathrm{MHD}}/V_{\mathrm{abl}} \approx 1$, i.e., a significant reduction in stabilization due to the self-generated magnetic fields for those modes. Future work will also quantify how the self-generated fields modify hot-spot temperature and fusion yield; this is of particular interest for the recent ignition experiment on the National Ignition Facility [54–56], which is expected to have generated more magnetic flux than previous experiments due to the larger hot-spot temperatures [37].

The theory deviates from simulations once the magnetic field detaches from the spike, which occurs when the ablative stabilization becomes so strong that the spike begins to decrease in size. At this stage the magnetic flux loops are injected into the hot plasma, which reduces the impact on Rayleigh-Taylor growth but continues to magnetize the local electron population and may still modify ICF hot-spot performance.

This work was performed under the auspices of the U.S. Department of Energy by Lawrence Livermore National Laboratory under Contract No. DE-AC52-07NA27344.

[1] H. J. Kull, Theory of the Rayleigh-Taylor instability, Phys. Rep. **206**, 197 (1991).

[2] Y. Zhou, Rayleigh-Taylor and Richtmyer-Meshkov instability induced flow, turbulence, and mixing. I, Phys. Rep. **720–722**, 1 (2017)

[3] Y. Zhou, T. T. Clark, D. S. Clark, S. G. Glendinning, M. A. Skinner, C. M. Huntington, O. A. Hurricane, A. M. Dimits, and B. A. Remington, Turbulent mixing and transition criteria of flows induced by hydrodynamic instabilities, Phys. Plasmas **26**, 080901 (2019).

[4] J. J. Hester, J. M. Stone, P. A. Scowen, B.-I. Jun, J. S. Gallagher III, M. L. Norman, G. E. Ballester, C. J. Burrows, S. Casertano, J. T. Clarke, D. Crisp, R. E. Griffiths, J. G. Hoessel, J. A. Holtzman, J. Krist, J. R. Mould, R. Sankrit, K. R. Stapelfeldt, J. T. Trauger, A. Watson, and J. A. Westphal, WFPC2 studies of the Crab Nebula. III. Magnetic Rayleigh-Taylor instabilities and the origin of the filaments, Astrophys. J. **456**, 225 (1996).

[5] W. H. Cabot and A. W. Cook, Reynolds number effects on Rayleigh–Taylor instability with possible implications for type Ia supernovae, Nat. Phys. **2**, 562 (2006).

[6] A. C. Calder, B. Fryxell, T. Plewa, R. Rosner, L. J. Dursi, V. G. Weirs, T. Dupont, H. F. Robey, J. O. Kane, B. A. Remington, R. P. Drake, G. Dimonte, M. Zingale, F. X. Timmes, K. Olson, P. Ricker, P. MacNeice, and H. M. Tufo, On validating an astrophysical simulation code, Astrophys. J. Suppl. Ser. **143**, 201 (2002).

[7] D. Arnett, The role of mixing in astrophysics, Astrophys. J. Suppl. Ser. **127**, 213 (2000).

[8] S. E. Bodner, Rayleigh-Taylor Instability and Laser-Pellet Fusion, Phys. Rev. Lett. **33**, 761 (1974).

[9] W. W. Hsing, Cris W. Barnes, J. B. Beck, N. M. Hoffman, D. Galmiche, A. Richard, J. Edwards, P. Graham, S. Rothman, and B. Thomas, Rayleigh–Taylor instability evolution in ablatively driven cylindrical implosions, Phys. Plasmas **4**, 1832 (1997).

[10] K. S. Raman, V. A. Smalyuk, D. T. Casey, S. W. Haan, D. E. Hoover, O. A. Hurricane, J. J. Kroll, A. Nikroo, J. L. Peterson, B. A. Remington, H. F. Robey, D. S. Clark, B. A. Hammel, O. L. Landen, M. M. Marinak, D. H. Munro, K. J. Peterson, and J. Salmonson, An in-flight radiography platform to measure hydrodynamic instability growth in inertial confinement fusion capsules at the National Ignition Facility, Phys. Plasmas **21**, 072710 (2014).

[11] V. A. Smalyuk, Experimental techniques for measuring Rayleigh–Taylor instability in inertial confinement fusion, Phys. Scr. **86**, 058204 (2012).

[12] V. A. Smalyuk, C. R. Weber, O. L. Landen, S. Ali, B. Bachmann, P. M. Celliers, E. L. Dewald, A. Fernandez, B. A. Hammel, G. Hall, A. G. MacPhee, L. Pickworth, H. F. Robey, N. Alfonso, K. L. Baker, L. F. Berzak Hopkins, L. Carlson, D. T. Casey, D. S. Clark, J. Crippen *et al.*, Review of hydrodynamic instability experiments in inertially confined fusion implosions on National Ignition Facility, Plasma Phys. Controlled Fusion **62**, 014007 (2020).

[13] D. S. Clark, C. R. Weber, J. L. Milovich, J. D. Salmonson, A. L. Kritcher, S. W. Haan, B. A. Hammel, D. E. Hinkel, O. A. Hurricane, O. S. Jones, M. M. Marinak, P. K. Patel, H. F. Robey, S. M. Sepke, and M. J. Edwards, Three-dimensional simulations of low foot and high foot implosion experiments on the National Ignition Facility, Phys. Plasmas **23**, 056302 (2016).

[14] D. S. Clark, C. R. Weber, J. L. Milovich, A. E. Pak, D. T. Casey, B. A. Hammel, D. D. Ho, O. S. Jones, J. M. Koning, A. L. Kritcher, M. M. Marinak, L. P. Masse, D. H. Munro, M. V. Patel, P. K. Patel, H. F. Robey, C. R. Schroeder, S. M. Sepke, and M. J. Edwards, Three-dimensional modeling and hydrodynamic scaling of National Ignition Facility implosions, Phys. Plasmas **26**, 050601 (2019).

[15] R. Betti, M. Umansky, V. Lobatchev, V. N. Goncharov, and R. L. McCrory, Hot-spot dynamics and deceleration-phase Rayleigh–Taylor instability of imploding inertial confinement fusion capsules, Phys. Plasmas **8**, 5257 (2001).

[16] C. R. Weber, D. S. Clark, A. W. Cook, D. C. Eder, S. W. Haan, B. A. Hammel, D. E. Hinkel, O. S. Jones, M. M. Marinak, J. L. Milovich, P. K. Patel, H. F. Robey, J. D. Salmonson, S. M. Sepke, and C. A. Thomas, Three-dimensional hydrodynamics of the deceleration stage in inertial confinement fusion, Phys. Plasmas **22**, 032702 (2015).

[17] D. T. Casey, B. J. MacGowan, J. D. Sater, A. B. Zylstra, O. L. Landen, J. Milovich, O. A. Hurricane, A. L. Kritcher, M. Hohenberger, K. Baker, S. Le Pape, T. Döppner, C. Weber, H. Huang, C. Kong, J. Biener, C. V. Young, S. Haan, R. C. Nora, S. Ross *et al.*, Evidence of Three-Dimensional Asymmetries Seeded by High-Density Carbon-Ablator Nonuniformity in Experiments at the National Ignition Facility, Phys. Rev. Lett. **126**, 025002 (2021).

[18] M. Gatu Johnson, P. J. Adrian, K. S. Anderson, B. D. Appelbe, J. P. Chittenden, A. J. Crilly, D. Edgell, C. J. Forrest, J. A. Frenje, V. Yu. Glebov, B. M. Haines, I. Igumenshchev, D. Jacobs-Perkins, R. Janezic, N. V. Kabadi, J. P. Knauer, B. Lahmann, O. M. Mannion, F. J. Marshall, T. Michel *et al.*, Impact of stalk on directly driven inertial confinement fusion implosions, Phys. Plasmas **27**, 032704 (2020).

[19] V. A. Smalyuk, S. V. Weber, D. T. Casey, D. S. Clark, J. E. Field, S. W. Haan, B. A. Hammel, A. V. Hamza, D. E. Hoover, O. L. Landen, A. Nikroo, H. F. Robey, and C. R. Weber, Hydrodynamic instability growth of three-dimensional, "native-roughness" modulations in x-ray driven, spherical implosions at the National Ignition Facility, Phys. Plasmas **22**, 072704 (2015).

[20] K. McGlinchey, B. Appelbe, A. Crilly, J. Tong, C. Walsh, and J. Chittenden, Diagnostic signatures of performance degrading perturbations in inertial confinement fusion implosions, Phys. Plasmas **25**, 122705 (2018).

[21] B. A. Hammel, R. Tommasini, D. S. Clark, J. Field, M. Stadermann, and C. Weber, Simulations and experiments of the growth of the "tent" perturbation in NIF ignition implosions, J. Phys.: Conf. Ser. **717**, 012021 (2015).

[22] C. K. Li, F. H. Séguin, J. A. Frenje, R. D. Petrasso, J. A. Delettrez, P. W. McKenty, T. C. Sangster, R. L. Keck, J. M. Soures, F. J. Marshall, D. D. Meyerhofer, V. N. Goncharov, J. P. Knauer, P. B. Radha, S. P. Regan, and W. Seka, Effects of Nonuniform Illumination on Implosion Asymmetry in Direct-Drive Inertial Confinement Fusion, Phys. Rev. Lett. **92**, 205001 (2004).

[23] M. Gatu Johnson, B. D. Appelbe, J. P. Chittenden, A. Crilly, J. Delettrez, C. Forrest, J. A. Frenje, V. Yu. Glebov, W. Grimble, B. M. Haines, I. V. Igumenshchev, R. Janezic, J. P. Knauer, B. Lahmann, F. J. Marshall, T. Michel, F. H. Séguin, C. Stoeckl, C. Walsh, A. B. Zylstra, and R. D. Petrasso, Impact of imposed mode 2 laser drive asymmetry on inertial confinement fusion implosions, Phys. Plasmas **26**, 012706 (2019).

[24] Brian K. Spears, M. J. Edwards, S. Hatchett, J. Kilkenny, J. Knauer, A. Kritcher, J. Lindl, D. Munro, P. Patel, H. F. Robey, and R. P. J. Town, Mode 1 drive asymmetry in inertial confinement fusion implosions on the National Ignition Facility, Phys. Plasmas **21**, 042702 (2014).

[25] J. Sanz, J. Ramírez, R. Ramis, R. Betti, and R. P. J. Town, Nonlinear Theory of the Ablative Rayleigh-Taylor Instability, Phys. Rev. Lett. **89**, 195002 (2002).

[26] K. S. Budil, B. A. Remington, T. A. Peyser, K. O. Mikaelian, P. L. Miller, N. C. Woolsey, W. M. Wood-Vasey, and A. M. Rubenchik, Experimental Comparison of Classical versus Ablative Rayleigh-Taylor Instability, Phys. Rev. Lett. **76**, 4536 (1996).

[27] R. Betti, V. N. Goncharov, R. L. McCrory, and C. P. Verdon, Self-consistent cutoff wave number of the ablative Rayleigh–Taylor instability, Phys. Plasmas **2**, 3844 (1995).

[28] R. Betti, V. N. Goncharov, R. L. McCrory, and C. P. Verdon, Growth rates of the ablative Rayleigh–Taylor instability in inertial confinement fusion, Phys. Plasmas **5**, 1446 (1998).

[29] J. D. Kilkenny, S. G. Glendinning, S. W. Haan, B. A. Hammel, J. D. Lindl, D. Munro, B. A. Remington, S. V. Weber, J. P. Knauer, and C. P. Verdon, A review of the ablative stabilization of the Rayleigh–Taylor instability in regimes relevant to inertial confinement fusion, Phys. Plasmas **1**, 1379 (1994).

[30] M. J. E. Manuel, C. K. Li, F. H. Séguin, J. Frenje, D. T. Casey, R. D. Petrasso, S. X. Hu, R. Betti, J. D. Hager, D. D. Meyerhofer, and V. A. Smalyuk, First Measurements of Rayleigh-Taylor-Induced Magnetic Fields in Laser-Produced Plasmas, Phys. Rev. Lett. **108**, 255006 (2012).

[31] L. Gao, P. M. Nilson, I. V. Igumenschev, G. Fiksel, R. Yan, J. R. Davies, D. Martinez, V. Smalyuk, M. G. Haines, E. G. Blackman, D. H. Froula, R. Betti, and D. D. Meyerhofer, Observation of Self-Similarity in the Magnetic Fields Generated by the Ablative Nonlinear Rayleigh-Taylor Instability, Phys. Rev. Lett. **110**, 185003 (2013).

[32] M. J. E. Manuel, M. Flaig, T. Plewa, C. K. Li, F. H. Séguin, J. A. Frenje, D. T. Casey, R. D. Petrasso, S. X. Hu, R. Betti, J. Hager, D. D. Meyerhofer, and V. Smalyuk, Collisional effects on Rayleigh-Taylor-induced magnetic fields, Phys. Plasmas **22**, 056305 (2015).

[33] D. W. Hill and R. J. Kingham, Enhancement of pressure perturbations in ablation due to kinetic magnetized transport effects under direct-drive inertial confinement fusion relevant conditions, Phys. Rev. E **98**, 021201(R) (2018).

[34] J. D. Sadler, C. A. Walsh, and H. Li, Symmetric Set of Transport Coefficients for Collisional Magnetized Plasma, Phys. Rev. Lett. **126**, 075001 (2021).

[35] C. A. Walsh, J. P. Chittenden, K. McGlinchey, N. P. L. Niasse, and B. D. Appelbe, Self-Generated Magnetic Fields in the Stagnation Phase of Indirect-Drive Implosions on the National Ignition Facility, Phys. Rev. Lett. **118**, 155001 (2017).

[36] B. Srinivasan, G. Dimonte, and X.-Z. Tang, Magnetic Field Generation in Rayleigh-Taylor Unstable Inertial Confinement Fusion Plasmas, Phys. Rev. Lett. **108**, 165002 (2012).

[37] C. A. Walsh and D. S. Clark, Biermann battery magnetic fields in ICF capsules: Total magnetic flux generation, Phys. Plasmas **28**, 092705 (2021).

[38] C. A. Walsh, J. D. Sadler, and J. R. Davies, Updated magnetized transport coefficients: Impact on laser-plasmas with self-generated or applied magnetic fields, Nucl. Fusion **61**, 116025 (2021).

[39] F. García-Rubio, R. Betti, J. Sanz, and H. Aluie, Magnetic-field generation and its effect on ablative Rayleigh–Taylor

instability in diffusive ablation fronts, Phys. Plasmas **28**, 012103 (2021).

[40] E. M. Epperlein and M. G. Haines, Plasma transport coefficients in a magnetic field by direct numerical solution of the Fokker–Planck equation, Phys. Fluids **29**, 1029 (1986).

[41] A. Ciardi, S. V. Lebedev, A. Frank, E. G. Blackman, J. P. Chittenden, C. J. Jennings, D. J. Ampleford, S. N. Bland, S. C. Bott, J. Rapley, G. N. Hall, F. A. Suzuki-Vidal, A. Marocchino, T. Lery, and C. Stehle, The evolution of magnetic tower jets in the laboratory, Phys. Plasmas **14**, 056501 (2007).

[42] J. P. Chittenden, N. P. Niasse, S. N. Bland, G. A. Hall, S. V. Lebedev, and C. A. Jennings, Recent advances in magneto-hydrodynamic modeling of wire array Z-pinches, in *2009 IEEE International Conference on Plasma Science - Abstracts* (IEEE, New York, 2009), p. 1-1.

[43] P. T. Campbell, C. A. Walsh, B. K. Russell, J. P. Chittenden, A. Crilly, G. Fiksel, P. M. Nilson, A. G. R. Thomas, K. Krushelnick, and L. Willingale, Magnetic Signatures of Radiation-Driven Double Ablation Fronts, Phys. Rev. Lett. **125**, 145001 (2020).

[44] J. D. Sadler, H. Li, and K. A. Flippo, Magnetic field generation from composition gradients in inertial confinement fusion fuel, Philos. Trans. R. Soc. A **378**, 20200045 (2020).

[45] M. Sherlock and J. J. Bissell, Suppression of the Biermann Battery and Stabilization of the Thermomagnetic Instability in Laser Fusion Conditions, Phys. Rev. Lett. **124**, 055001 (2020).

[46] P. T. Campbell, C. A. Walsh, B. K. Russell, J. P. Chittenden, A. Crilly, G. Fiksel, L. Gao, I. V. Igumenshchev, P. M. Nilson, A. G. R. Thomas, K. Krushelnick, and L. Willingale, Measuring magnetic flux suppression in high-power laser-plasma interactions, Phys. Plasmas **29**, 012701 (2022).

[47] C. A. Walsh, J. P. Chittenden, D. W. Hill, and C. Ridgers, Extended-magnetohydrodynamics in under-dense plasmas, Phys. Plasmas **27**, 022103 (2020).

[48] P. Sharma and G. W. Hammett, Preserving monotonicity in anisotropic diffusion, J. Comput. Phys. **227**, 123 (2007).

[49] C. A. Walsh, Extended magneto-hydrodynamic effects in indirect-drive inertial confinement fusion experiments, Ph.D. thesis, Imperial College, 2018.

[50] J. R. Davies, H. Wen, J.-Y. Ji, and E. D. Held, Transport coefficients for magnetic-field evolution in inviscid magneto-hydrodynamics, Phys. Plasmas **28**, 012305 (2021).

[51] S. Faik, A. Tauschwitz, and I. Iosilevskiy, The equation of state package FEOS for high energy density matter, Comput. Phys. Commun. **227**, 117 (2018).

[52] C. A. Walsh, Magnetized ablative Rayleigh-Taylor instability in three dimensions, Phys. Rev. E **105**, 025206 (2022).

[53] C. Walsh, R. Florido, M. Bailly-Grandvaux, F. Suzuki-Vidal, J. P. Chittenden, A. Crilly, M. A. Gigosos, R. Mancini, G. Perez-Callejo, C. Vlachos, C. McGuffey, F. N. Beg, and J. J. Santos, Exploring extreme magnetization phenomena in directly-driven imploding cylindrical targets, Plasma Phys. Control. Fusion, **64**, 025007 (2022).

[54] H. Abu-Shawareb, R. Acree, P. Adams, J. Adams, B. Addis, R. Aden, P. Adrian, B. B. Afeyan, M. Aggleton, L. Aghaian, A. Aguirre, D. Aikens, J. Akre, F. Albert, M. Albrecht, B. J. Albright, J. Albritton, J. Alcala, C. Alday, D. A. Alessi *et al.*, Lawson Criterion for Ignition Exceeded in an Inertial Fusion Experiment, Phys. Rev. Lett. **129**, 075001 (2022).

[55] A. L. Kritcher, A. B. Zylstra, D. A. Callahan, O. A. Hurricane, C. R. Weber, D. S. Clark, C. V. Young, J. E. Ralph, D. T. Casey, A. Pak, O. L. Landen, B. Bachmann, K. L. Baker, L. Berzak Hopkins, S. D. Bhandarkar, J. Biener, R. M. Bionta, N. W. Birge, T. Braun, T. M. Briggs *et al.*, Design of an inertial fusion experiment exceeding the Lawson criterion for ignition, Phys. Rev. E **106**, 025201 (2022).

[56] A. B. Zylstra, A. L. Kritcher, O. A. Hurricane, D. A. Callahan, J. E. Ralph, D. T. Casey, A. Pak, O. L. Landen, B. Bachmann, K. L. Baker, L. Berzak Hopkins, S. D. Bhandarkar, J. Biener, R. M. Bionta, N. W. Birge, T. Braun, T. M. Briggs, P. M. Celliers, H. Chen, C. Choate *et al.*, Experimental achievement and signatures of ignition at the National Ignition Facility, Phys. Rev. E **106**, 025202 (2022).